

Modeling of nucleation, growth, dissolution, and disappearance of paracetamol in ethanol solution for unseeded batch cooling crystallization with temperature-cycling strategy

Youngjo Kim,[†] Yoshiaki Kawajiri,^{†,‡} Ronald W. Rousseau,[†] and Martha A.
Grover^{*,†}

[†]*School of Chemical and Biomolecular Engineering, Georgia Institute of Technology,
Atlanta, GA, 30031*

[‡]*Department of Materials Process Engineering, Nagoya University, Nagoya, Aichi,
464-8603, Japan*

E-mail: martha.grover@chbe.gatech.edu

Abstract

A population balance model (PBM) is developed for unseeded batch crystallization, with *temperature-cycling strategies* to control the crystal size distribution. The model is able to predict the evolution of crystal size distributions of crystallizing paracetamol from ethanol solutions considering the characteristics of primary nucleation, secondary nucleation, growth, dissolution, and disappearance of crystals. Process analytical technology (PAT) tools were employed to collect solute concentration data and crystal size

distribution data. This model employs a boundary condition to describe the disappearance of crystals in temperature-cycling strategies where the temperature is increased and decreased repeatedly. As a result, the obtained model can describe the evolution of crystal size distribution when repetition of cooling and heating is carried out. Moreover, this model can be applied to investigate phenomena that are challenging to explain with experimental data alone, thereby we can gain insight and optimize the operation of the process.

Introduction

Separation and purification are critical steps in the production of many chemical products. Among numerous separation processes, crystallization is used extensively in the food, chemical, and pharmaceutical industries. Crystallization can be operated in a batch or continuous manner according to the manufacturing scale or change of product grades. Batch crystallization processes are often used because they have many advantages such as simple facilities, low installation cost, and flexibility in a product change.¹

Crystallization is mainly affected by the supersaturation in the solution. In order to control product characteristics and the crystallization process, process variables are manipulated such as the supersaturation, system temperature, pH of the solution, system pressure, amount of anti-solvent, and so on. Among various ways to control the supersaturation, cooling crystallization can be performed by adjusting only a single control variable, temperature, without an addition of another component.²

Temperature cycling has been employed in batch crystallization processes to control many crystal properties such as crystal size and distribution,³⁻⁶ shape,^{7,8} polymorphic form,^{9,10} and chirality of crystals.^{11,12} Cycling the temperature leads to dissolution and recrystallization, so that the system can eliminate small undesired crystals. As reported by Wu *et al.*,¹³ a temperature-cycling strategy can be classified into the following three categories: 1) continuous dissolution in equipment external to the crystallizer, 2) sequential heating and cooling

in the crystallizer, and 3) simultaneous heating and cooling at different locations in a single crystallizer. Among these three categories, the second approach is used here because of the simplicity in the experimental setup.

Among various crystal qualities, a uniform crystal size and narrow size distribution improve the efficiency of filtration in commercial processes.^{2,14} Mathematical modeling can reduce the experimental efforts and time needed to optimize temperature profiles for obtaining a desired crystal size distribution. Such models should include nucleation and growth of crystals, and also may include agglomeration, breakage, and attrition. However, the main mechanisms that affect the final crystal product qualities are nucleation and growth.² Moreover, the dissolution and disappearance of crystals take place as well when the temperature-cycling strategy is employed. Hence, the model must describe the disappearance of crystals as well as nucleation, growth, and dissolution in order to model attributes of crystallization by temperature cycling. In this study, a full population balance model (PBM) is used to describe the crystallization in a batch process. While many studies have examined primary nucleation, secondary nucleation and growth,^{14–18} few modeling studies involving disappearance of crystals are found in the literature.^{3,19,20}

Most PBMs cannot be solved analytically except for very simple cases. Therefore, various techniques have been employed to solve the PBM numerically, which include method of moments,^{21–23} method of characteristics,^{24,25} finite-element method (FEM),²⁶ finite-volume method (FVM),^{27–29} and the conservation element/solution element (CE/SE).^{17,30} Qamar *et al.*³¹ compares various numerical methods to solve the PBM, and the CE/SE scheme demonstrated “much better performance” among tested approaches.

The present study aims to develop and validate a mathematical model of unseeded crystallization of paracetamol from an ethanolic solution in a batch process employing a temperature-cycling strategy. The model handles kinetics of primary and secondary nucleation, growth and dissolution of crystals, and disappearance of fines. Experiments that apply temperature-cycling strategies were carried out to estimate kinetic parameters. Each

experiment employed process analytical technology (PAT) tools such as focused beam reflectance measurement (FBRM) and attenuated total reflectance-Fourier transform infrared (ATR-FTIR) spectroscopy to measure properties of particles and solution, respectively. The final crystal size distribution was analyzed by an *ex situ* method, sieve analysis after washing and drying crystals.

Modeling

Population Balance Model

The one-dimensional population balance model can describe the well-mixed batch crystallization system.^{14,17} If agglomeration and breakage of crystals can be ignored, the population balance equation can be expressed as

$$\frac{\partial n}{\partial t} + G \frac{\partial n}{\partial L} = 0 \quad (1)$$

where n represents the number density of crystals [$\#/(\mu\text{m}\cdot\text{kg of solvent})$], G denotes the growth rate of crystals [$\mu\text{m}/\text{min}$], t is the time [min], and L is the characteristic crystal size [μm]. Equation (1) is based on assumptions that the crystal shape does not depend on the crystal size and the growth rate is size-independent and without dispersion. The initial condition and the boundary condition for batch crystallization from a clear solution are

$$n(t, L = 0) = \frac{B}{G}, \quad S \geq 1 \quad (2)$$

$$n(t = 0, L) = n_0 \quad (3)$$

where B denotes the nucleation rate [$\#/(\text{min}\cdot\text{kg of solvent})$], n_0 is the initial number density for each crystal size domain, and S is the supersaturation, which is defined as the concen-

tration in the solution, c , over the saturated concentration at the system temperature, c_s . New nuclei are assumed to appear only in the smallest size domain. In the initial condition, Equation (3), where G is independent of L , n_0 is zero in the entire domain from 0 to L_{\max} for unseeded crystallization since this process begins with a clear solution.

The nucleation rate, B , can be divided into primary and secondary nucleation. Primary nucleation is the mechanism in which crystals are formed from a clear solution (i.e. does not have any crystals). On the other hand, secondary nucleation models the mechanism where formation of new nuclei is caused by existing crystals.³²

According to classical nucleation theory (CNT), the homogeneous primary nucleation rate is given by the surface free energy change of nuclei and the free energy change on the phase transformation.

$$B_1 = \begin{cases} k_{b1} \exp \left(-\frac{16\pi\nu^3\sigma^3}{3k^3T^3(\ln S)^2} \right), & S \geq 1 \\ 0, & S < 1 \end{cases} \quad (4)$$

where k_{b1} is a pre-exponential rate constant [$\#/(\text{min} \cdot \text{kg solvent})$], ν is the volume of one solute molecule [m^3], σ is the interfacial energy between crystal and solution [J/m^2], k is the Boltzmann constant [$\text{m}^2\text{kg}/\text{s}^2/\text{K}$], T is the system temperature [K]. In this paper, k_{b1} and σ are handled as parameters, T and S are provided by experimental measurements, and v is calculated with the molecular weight and density of the solid solute.

In this study, the secondary nucleation rate, B_2 , is described by an empirical model:

$$B_2 = \begin{cases} k_{b2} (S - 1)^\alpha m_s^\beta, & S \geq 1 \\ 0, & S < 1 \end{cases} \quad (5)$$

where k_{b2} is the pre-exponential rate constant [$\#/(\text{min} \cdot \text{kg solvent})$], m_s is the mass of crystals in the unit mass of solution [$\text{g-solute}/\text{g-solvent}$], and α and β are the exponential parameters for the model. In this model, secondary nucleation is determined by the supersaturation

of the solution and mass of crystals in the slurry. The secondary nucleation is known to be affected by collisions among crystals in the system according to the stirring rate,^{33–36} so we used a constant stirring speed to minimize this effect. The total nucleation rate, B , is determined by

$$B = B_1 + B_2 \quad (6)$$

In this study, size-independent growth and dissolution were assumed.^{14,17} Hence, growth and dissolution rates of crystals can be expressed similarly as functions of temperature and the absolute supersaturation.

$$G = k_g \exp \left(-\frac{E_{a_g}}{RT} \right) (c - c_s)^{\gamma_g}, \quad c \geq c_s \quad (7)$$

$$D = k_d \exp \left(-\frac{E_{a_d}}{RT} \right) (c_s - c)^{\gamma_d}, \quad c < c_s \quad (8)$$

where D is the dissolution rate of crystals $[(\mu\text{m}/\text{min})]$, k_g and k_d are the pre-exponential rate constants for the crystal growth $[(\mu\text{m}/\text{min})(\text{g-solute}/\text{g-solvent})^{-\gamma_g}]$ and dissolution $[(\mu\text{m}/\text{min})(\text{g-solute}/\text{g-solvent})^{-\gamma_d}]$, respectively, E_{a_g} and E_{a_d} are the activation energies $[\text{J}/\text{mol}]$ for growth and dissolution, γ_g and γ_d are exponential parameters on supersaturation for the growth and dissolution, respectively, and R is the universal gas constant $[\text{J}/\text{mol}/\text{K}]$. Crystals grow when the concentration of the solution is higher than solubility, but crystals dissolve into the solution under the opposite condition. Therefore, $c - c_s$ and $c_s - c$ determine the growth and dissolution of crystals in the model, respectively.

Disappearance of crystals in the PBM

If the concentration in the solution is kept lower than the solubility, crystals dissolve continuously and some small crystals may disappear, so it is necessary that the PBM framework describes disappearance as well as dissolution of crystals. In order to describe the disappear-

ance of crystals, various criteria such as the critical size of crystals,¹⁹ detection limit,³ and physically minimum size of crystals^{20,37} have been applied to describe the disappearance of crystals. In this study, an additional boundary condition is introduced to describe crystal disappearance:

$$n(t, L \leq 0) = 0, \quad S < 1 \quad (9)$$

Numerical method

In this work, the ‘space-time conservation element and solution element’ (CE/SE) method was employed to obtain the solution of the PBM. This scheme was originally developed to solve Navier-Stokes and Euler equations,³⁸ and it has been applied to solve many partial differential equations in fields such as magnetohydrodynamics,³⁹ heat transfer,^{40,41} adsorption,^{42,43} and crystallization.^{17,20,30,31,37,44,45} Motz *et al.*³⁰ showed the CE/SE method can provide more accurate and faster solutions for the PBM than those given by the FVM, with fewer grid points. Also, Qamar *et al.*³¹ reported that the CE/SE method presents faster estimation and more accurate results than all other presented schemes such as the high resolution semi-discrete FVM and PARSIVAL. In particular, the CE/SE scheme accurately simulated the sharp peaks and discontinuities.

In this study, an artificial size domain that has a negative value of L , which is the bin size in the model, was employed to describe the disappearance of crystals as shown in Figure 1. The change of the number density distribution illustrates when dissolution occurs. The initial density distribution (blue) moves left in Figure 1 because the crystal sizes decrease during the dissolution phase. As a result, fine crystals disappear and a part of the final density distribution (red) moves into the negative size domain. Because crystals cannot have negative sizes, number densities of crystals having size less than or equal to zero are removed in the model.

In order to describe the crystallization system including crystallization, dissolution, and

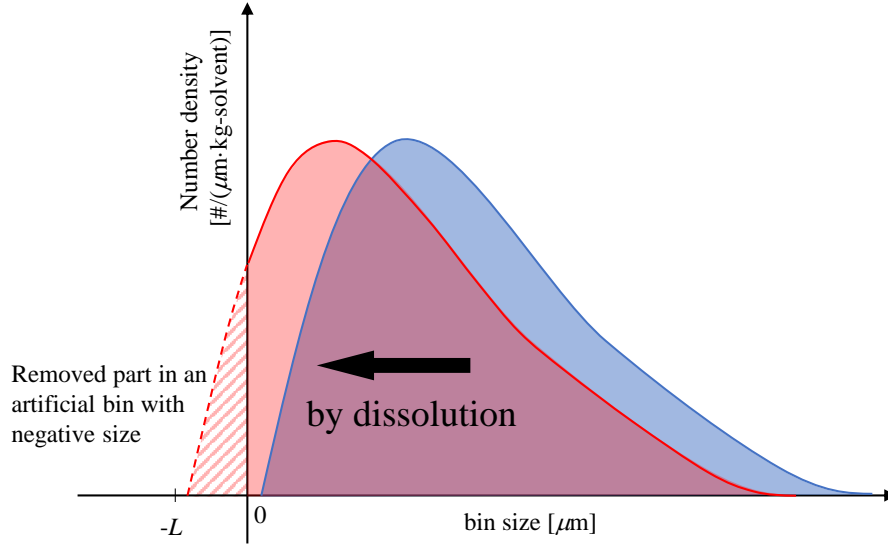


Figure 1: Concept of the negative cell in the PBM. The blue and red distribution represent the initial and final number density distribution, respectively. The initial distribution moves left by dissolution and the disappeared crystals, which are expressed as the hatched pattern, are removed.

disappearance of crystals, the CE/SE scheme was coded in MATLAB[™] R2019b for a size range from $-\Delta L \mu\text{m}$ to $1000 \mu\text{m}$ with evenly spaced bins of ΔL , where ΔL is $5 \mu\text{m}$. The grid from $-5 \mu\text{m}$ to $0 \mu\text{m}$ is the pseudo spatial domain to describe the disappearance of crystals when the solution becomes undersaturated.

Estimation of mean crystal size

More than 20 different methods have been reported to evaluate the mean crystal size.⁴⁶ Among these methods, the volume mean crystal size is frequently used to evaluate the mean crystal size.⁴⁶ Assuming the crystal density is constant, the definition of volume mean crystal size is

$$\bar{L}_v = \frac{\sum n_i L_i^4}{\sum n_i L_i^3} = \frac{\sum (M_i L_i)}{\sum M_i} \approx \frac{\mu_4}{\mu_3} \quad (10)$$

where \bar{L}_v represents the volume mean crystal size; n , L , and M are the number density of

crystals, geometric mean crystal size, and mass of crystals, respectively; and subscript i is the size bin number. In this study, mean crystal sizes for crystallization and dissolution were estimated based on Equation (10) to compare the experimental and predicted results and to estimate dissolution parameters.

Parameter estimation

In this study, parameter estimation was carried out for crystallization and dissolution by minimizing the sum of squared relative errors between results from experiments and model predictions. The minimization problems were solved by the `fmincon` function which is an SQP solver⁴⁷ in MATLABTM R2019b.

Parameters for the primary nucleation, secondary nucleation, growth, and dissolution of crystals were obtained using the following objective function based on the concentration and the final volume density distribution:

$$\Phi_c(\theta_c) = w_c \sum_{i=1}^{N_r} \sum_{j=1}^{N_{d,i}} \frac{1}{N_{d,i}} \left(\frac{\hat{c}_{ij} - c_{ij}(\theta_c)}{\hat{c}_{ij}} \right)^2 + \sum_{i=1}^{N_r} \sum_{k=1}^{N_{m,v}} \frac{1}{N_{m,v}} \left(\frac{\hat{v}_{ik} - v_{ik}(\theta_c)}{\hat{v}_{ik}} \right)^2 \quad (11)$$

where $\theta_c = \{k_{b1}, \sigma, k_{b2}, \alpha, \beta, k_g, E_{ag}, \gamma_g, k_d, E_{ad}, \gamma_d\}$ is the parameter set for nucleation, growth, and dissolution kinetics, N_r is the number of experimental runs, $N_{d,i}$ is the number of sampled data for i^{th} run, N_{mv} is the number of size ranges for volume density distribution, c and v represent concentration and volume density distribution term, respectively; w_c is the weight for the term of concentration; \hat{c}_{ij} and c_{ij} are the measured and predicted concentrations; and \hat{v}_i and v_i are the measured and predicted final volume density distribution from each run.

The PBM was solved by the CE/SE method which can solve partial differential equations efficiently. However, because the time grid of the CE/SE method does not necessarily match the time points in the experimental data, the solution of the model is interpolated. Similarly, for the final volume density distribution, the sieving analysis has 11 unequally spaced bins

while the model has equally spaced finite elements which are 5 μm . Thus, the crystal size, L , was integrated over multiple size ranges that match the size bins in the sieve analysis.

Uncertainty in the model parameters can be quantified via confidence intervals. To estimate confidence intervals accurately, uncertainty in the experimental measurement must be quantified, which requires repetition of experiments. For this problem, an alternative method given by Bard et al.,⁴⁸ which is employed for crystallization by Li *et al.*¹⁷ and Rawlings *et al.*,⁴⁹ was used for approximation of the confidence intervals for estimated parameters.

$$(\boldsymbol{\theta} - \hat{\boldsymbol{\theta}})^T (V_{\boldsymbol{\theta}})^{-1} (\boldsymbol{\theta} - \hat{\boldsymbol{\theta}}) \leq \chi_{N_p, \alpha}^2 \quad (12)$$

The confidence intervals for each parameter, $\hat{\boldsymbol{\theta}}$, are calculated by Equation (12) with an assumption that the sum of squared errors follows a chi-square distribution. The degree of freedom, N_p , is the number of parameters, and α is 0.05 in 95% confidence for the chi-squared distribution:

$$(V_{\boldsymbol{\theta}})^{-1} = \sum_q (V_{\boldsymbol{\theta}}^q)^{-1} = \sum_j (B_q^j)^T (V^q)^{-1} (B_q^j), \quad q \in \{c, sv\} \quad (13)$$

where $V_{\boldsymbol{\theta}}$ is a covariance matrix of parameters, $\boldsymbol{\theta}$, from different measured data for concentration, sieved results for the crystallization, which are represented by c and sv , respectively, B^j is a $N_m \times N_p$ matrix of the sensitivities, $N_m = N_c + N_v$ is the total number of measured variables, $dy/d\theta$, of the n th sample, and V is the diagonal covariance matrix of the measurements. V and B_k^j can be estimated by Equations (14) and (15):

$$V_{ii}^q = \frac{1}{N_{d,q}} \sum_i^{N_{d,q}} e_{i,q}^2, \quad q \in \{c, sv\} \quad (14)$$

where $N_{d,q}$ is the number of samples for each measurement, e_i^2 is the squared error between experimental data and predicted results using $\hat{\boldsymbol{\theta}}$, e.g. $e_{i,c}^2 = (\hat{c}_i - c_i(\hat{\boldsymbol{\theta}}))^2$ for concentration. The sensitivity matrix, B_k^j is approximated by the finite difference method.

$$B_{k,q}^j = \left. \frac{\partial y_j}{\partial \theta} \right|_{\theta=\hat{\theta}} \approx \frac{y_{k,q}^j(\hat{\theta} + h_k \mathbf{e}_k) - y_{k,q}^j(\hat{\theta})}{h_k}, \quad k = 1, 2, \dots, N_m, \quad q \in \{c, sv\} \quad (15)$$

where $y_{k,q}^j$ is simulated result according to parameters, h_k is perturbation to $\hat{\theta}$, and \mathbf{e}_k is an $1 \times N_p$ unit vector. In this work, $N_{m,c} = 1$ for concentration and $N_{m,v} = 11$ for sieving and, $N_p = 11$ for the number of parameters. The degree of perturbation, h_k , is 0.1% of the magnitude in each element of $\hat{\theta}$.

Experimental Section

Materials and Apparatus

Crystallization and dissolution experiments for paracetamol (Sigma-Aldrich, > 99%) were performed in ethanol (KOPTEC, 200 proof anhydrous) in a 250-ml glass crystallizer with a pitched four-blade stirrer and temperature controller. The equipment, which is shown in Figure 2, includes three sensors which are Attenuated Total Reflectance-Fourier Transform Infrared (ATR-FTIR), Focused-Beam Reflectance Measurements (FBRM), and temperature sensors to measure characteristics of solutions and crystals in the crystallizer. The crystallization system, Optimax™ from Mettler-Toledo, can control the experimental conditions via a connected computer and software, iControl™ 6.0 by Mettler-Toledo. The ATR-FTIR, ReactIR iC10™ by Mettler-Toledo, measured the IR spectrum for wavenumbers from 650 to 3000 cm^{-1} every 30 seconds. The ATR-FTIR equipment was purged by compressed air purged and cooled down by liquid nitrogen before every measurement. Measured IR absorbance data were collected through software, iCIR™ by Mettler-Toledo. The concentration of the solution was evaluated based on measured IR absorbance data with a calibration model; further detail is provided later in the calibration section. The FBRM equipment, ParticleTrack G400™ by Mettler-Toledo, was set in the macro mode with the laser focus

distance of 0 μm and a scanning speed of 2 m/s. The FBRM measures the chord length every 30 seconds, and the computer and the software, iCFBRMTM by Mettler-Toledo, analyzed the chord length distributions (CLD). The software divides the chord size from 1 μm to 1000 μm into 100 bins via a logarithmic scale and generates the chord length histogram for each measurement. The range of experimental temperature was from 0 to 70 $^{\circ}\text{C}$ and every experiment was performed with a constant stirring rate of 400 rpm. When we needed to control the crystallization based on the supersaturation, iDataShareTM by Mettler-Toledo, which is an add-on package on MS ExcelTM, was utilized to convert IR absorbance to the concentration and import converted values into iControlTM software in real-time.

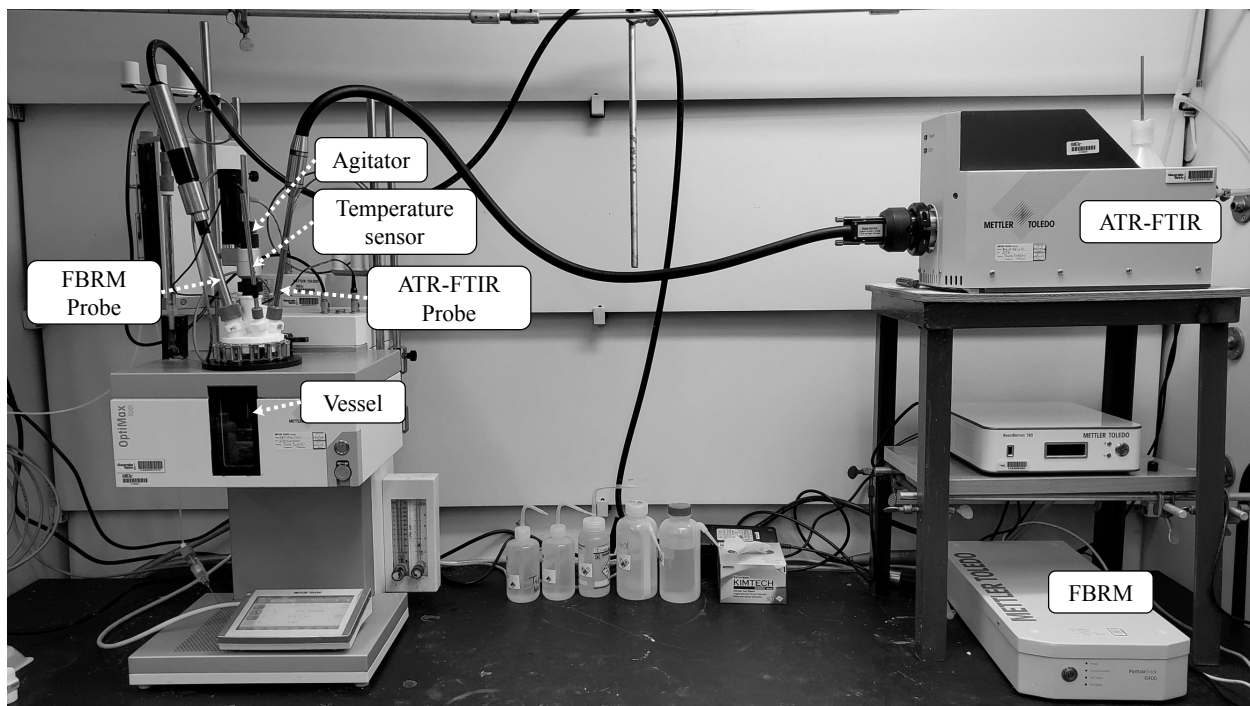


Figure 2: OptiMax system from Mettler Toledo equipped with probes for focused beam reflectance measurements (FBRM) and attenuated total reflectance Fourier transform infrared (ATR-FTIR) measurements.

Calibration for solution concentration

The concentration of the paracetamol solution was estimated by the measured IR absorbance data and a calibration model. In this study, we used mass fraction between the paracetamol

and ethanol, consistent with previous studies.^{3,8,14,17,50} Generally, the definition of a solution concentration is the mass or mole of a solute divided by the volume of a solution. However, it is difficult to track the accurate volume of a solution because it depends on the dissolved amount of solute. Thus, the unit of g-solute/g-solvent or g-solute/kg-solvent was employed. Here, a univariate approach was applied to infer the characteristics of crystallization because only two species affect the concentration of the solution; univariate approaches usually use peak heights, integrated peak area, or ratio of peak heights or area.⁵¹ In this study, the calibration model is based upon the ratio of peak heights of each material on the FTIR spectrum because the peak height of paracetamol increases, and the peak height of ethanol decreases when the paracetamol concentration increases. According to the previous research,¹⁷ the wavenumbers of ethanol and paracetamol are 1048 cm^{-1} and 1667 cm^{-1} , respectively as shown in Figure 3. However, the FTIR signals depend on various conditions such as probe alignment, contact of liquid and probe, and background absorbance.⁵² To handle this problem, the peak at 1800 cm^{-1} , which is not affected by the concentration of paracetamol and ethanol, was used as a reference peak. The concentrations of ethanol and paracetamol were given by normalizing two peaks, at 1048 and 1667 cm^{-1} , by that of the reference peak. The information to be estimated from the ATR-FTIR is the concentration of paracetamol in the ethanol solution. This concentration is based on the ratio between these two species, so the ratio of peak heights for paracetamol and ethanol was applied to determine the concentration in the solution.

A set of experiments was performed to relate the response of the peak height ratio of IR absorbance to the actual concentration and temperature change. Figure 4 shows that the ratio of peak heights changes according to the temperature of the solution even when the concentration of the solution is constant. Hence, the influence of temperature should be considered in the calibration model between the ratio of IR peak heights and concentration. The calibration model is

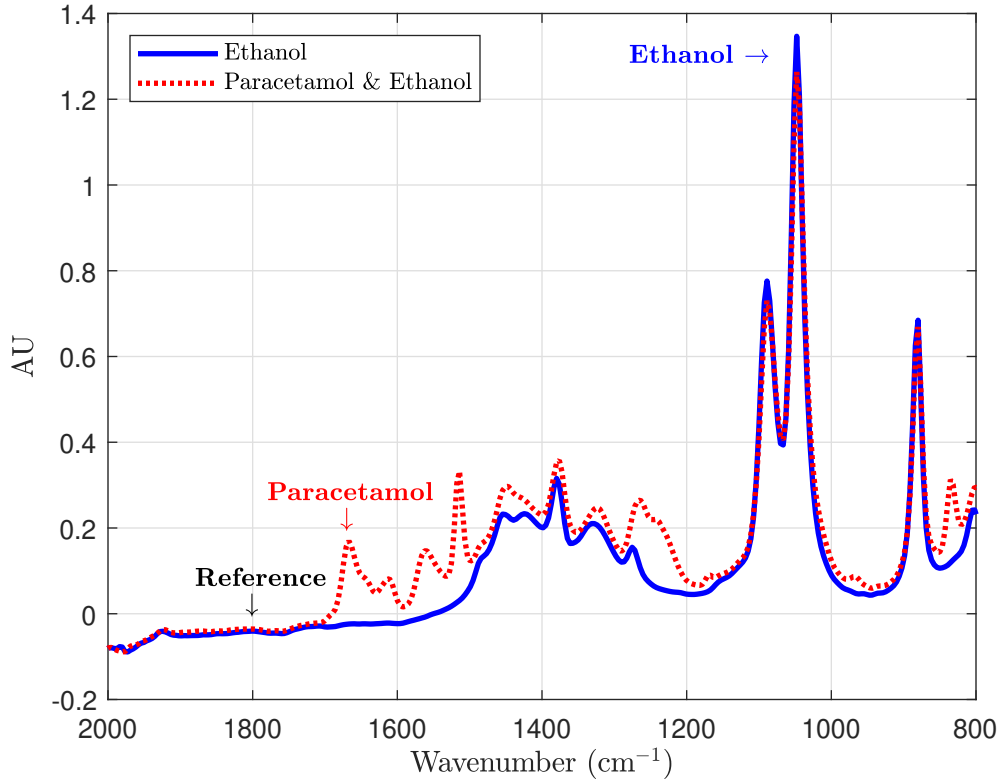


Figure 3: IR spectra for pure ethanol and paracetamol solution. Peaks at 1048 cm^{-1} and 1667 cm^{-1} represent ethanol and paracetamol, respectively.

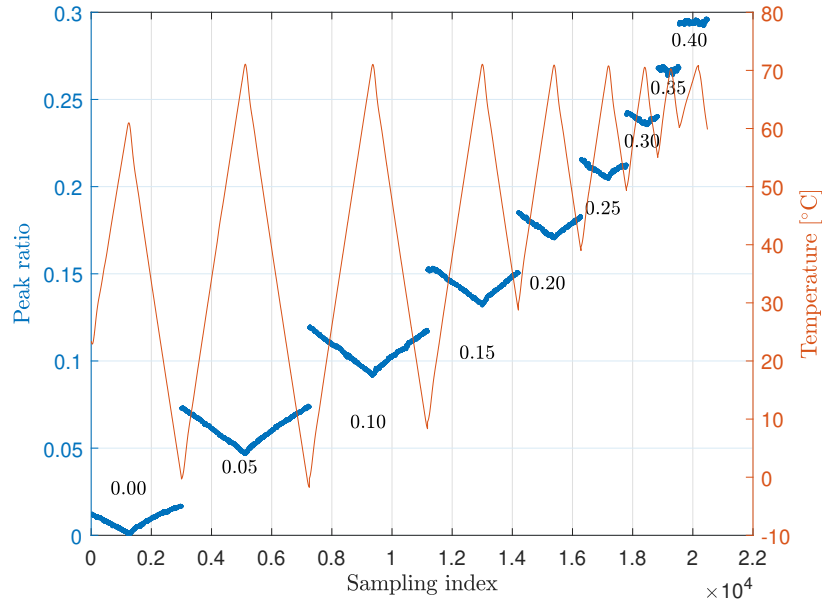


Figure 4: Change of IR peak height ratio based on temperature. Values shown together with the peak ratios are the actual concentration of the solution. Peak height ratio has a nonlinear relationship with the solution concentration and the system temperature.

$$h = k_1X^2 + k_2XT + k_3X + k_4T + k_5T^2 + k_6 \quad (16)$$

where h is the FTIR peak height for paracetamol (1667 cm^{-1} of wavelength) divided by the peak height for ethanol (1048 cm^{-1} of wavelength), based on reference peak height of 1800 cm^{-1} of wavelength. Here, X is the mole fraction of paracetamol in the ethanolic solution, and T [K] represents the temperature of the system. The sensitivity of ATR-FTIR depends on the environmental conditions in the lab, so calibration is carried out periodically to obtain accurate parameters for Equation (16).

Solubility of paracetamol in ethanol

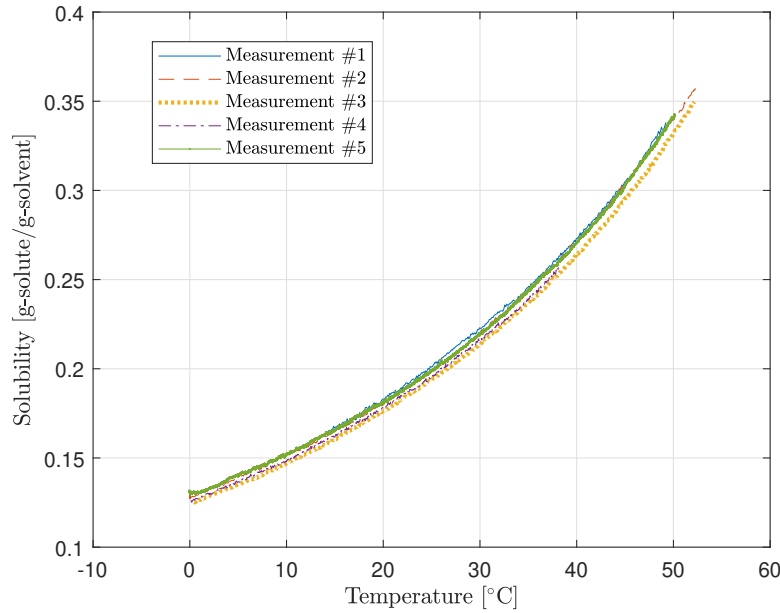


Figure 5: Five sets of solubility measurement data for paracetamol in the ethanol solution.

Solubility of paracetamol in ethanol was determined by five sets of continuous dissolution experiments by increasing temperature slowly. Each dissolution experiment was performed on a different day and the measured data varied slightly. Figure 5 shows the result of the solubility measurements. Solubility data sets have similar trends, and the average values

of these data sets was used to correlate the solubility of paracetamol in ethanol, c_s [g-paracetamol/g-ethanol], as the following polynomial equation

$$c_s = -8.707 + 9.669 \times 10^{-2}T - 3.610 \times 10^{-4}T^2 + 4.590 \times 10^{-7}T^3 \quad (17)$$

Volume shape factor

It is difficult to determine the volume of the paracetamol crystal directly because of its complicated shape. Hence, a volume shape factor has been used to approximate the volume and mass of crystals.⁵³ Generally, the shape factor, k_v , is defined as follows:

$$k_v = \frac{V}{L^3} = \frac{m_c}{\rho L^3} \quad (18)$$

where k_v is the volume shape factor of crystals, V is the actual volume of crystals [m^3], L is the size of crystals [m], m_c is the mass of crystals [kg], and ρ is the crystal density [kg/m^3].

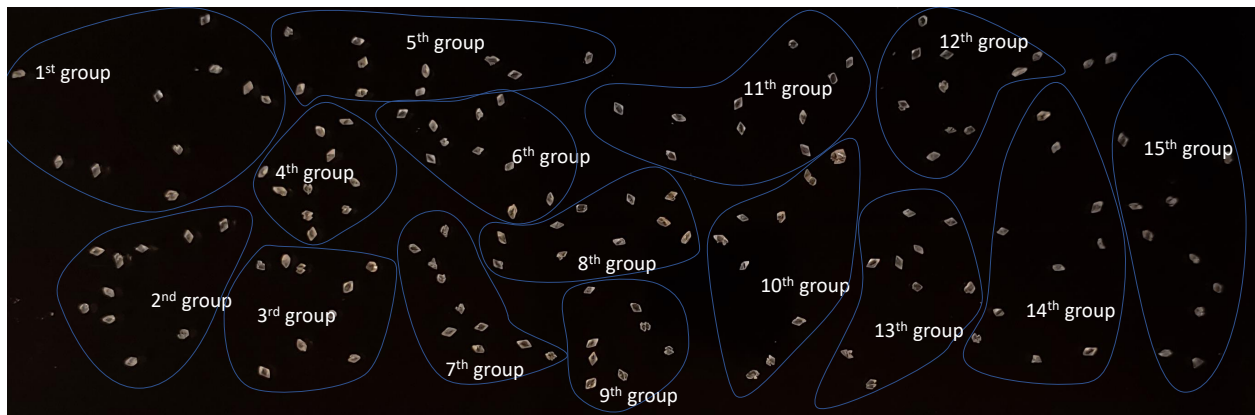


Figure 6: An example of the measurement of the volume shape factor of crystals. In this example, the crystal sizes are between $355 \mu\text{m}$ and $425 \mu\text{m}$, and the geometric mean crystal size of two boundaries, $388.4 \mu\text{m}$, represents all crystal sizes. In order to count crystals easier, crystals were grouped into bundles of ten crystal each. The mass of the 152 crystals is 7.68 mg .

The volume shape factor of paracetamol crystal was obtained by optical observations. Because the density of paracetamol crystals is already reported,⁵⁴ measured crystal size and mass can provide the shape factor, via Equation (18). As shown in Figure 6, the mass and

number of sieved crystals were measured to estimate the shape factors. In this work, 19 observations were carried out with crystals from seven different sieve size ranges of trays with 106–150, 150–212, 212–250, 355–420, 420–500, 500–600, and 600–850 μm , resulting in a shape factor of 0.797, which is close to 0.866 obtained by Worlitschek and Mazzotti.¹⁴

Crystallization with temperature cycling

The experiments applied a temperature plateau to minimize the effect of stochasticity of primary nucleation, in the same manner as in Li *et al.*¹⁷ The stirring speed in this system was fixed as 400 rpm to minimize bubble formation while maintaining mass and heat transfer in the system. The initial temperature of the system was set higher than the saturation temperature of the initial concentration so that the initial solution was undersaturated. The system temperature was decreased until the supersaturation reached the target value, with $-1.0\text{ }^{\circ}\text{C}/\text{min}$ as the cooling rate. The time when the decrease in temperature begins was considered as the initial time for the modeling. Next, the system was kept on the plateau temperature between 60 and 150 minutes, based on the status of crystals in the solution. The first appearance and growth of crystals took place during this temperature plateau. After this step, the temperature-cycling strategy was employed to obtain crystals with different mean sizes and size distributions. Each experiment had different initial concentrations and supersaturations on the temperature plateau. The plateau temperature was determined by the initial concentration and the target supersaturation. The concentration of paracetamol in the solution was evaluated based on the *in situ* ATR-FTIR measurement.

Results

Results of crystallization experiments with temperature cycling

In this study, six experiments were performed, and the conditions and the results are shown in Table 1. The initial concentrations, c_{ini} , are between 0.245 and 0.378 g-solute/g-solvent.

The supersaturation values at the plateau temperatures, S_{plat} , are chosen among 1.2, 1.3, and 1.4. The plateau temperatures, T_{plat} , were set based on the initial concentration and target supersaturation during the plateau time, t_{plat} . The final mass of recovered crystals, m_{fin} , was measured after the washing and drying procedures and is related to the initial and final concentrations by a mass balance. The final volume-weighted mean crystal size, \bar{L}_{fin} , is estimated using the results of sieving analysis.

Table 1: Conditions and measured results of crystallization experiments

	Exp.	Desired c_{ini} [g-solute /g-solvent]	Measured c_{ini} [g-solute /g-solvent]	Desired S_{plat} [-]	Measured S_{plat} [-]	T_{plat} [°C]	t_{plat} [min]	T_{fin} [°C]	m_{fin} [g]	\bar{L}_{fin} [μm]
Training sets	1	0.300	0.308	1.40	1.41	30.0	120	10.7	15.6	317.4
	2	0.250	0.245	1.30	1.27	24.0	150	19.9	7.25	259.7
	3	0.350	0.348	1.20	1.18	44.3	150	25.9	14.2	451.7
Test sets	4	0.370	0.378	1.40	1.40	40.0	60	6.7	22.1	307.6
	5	0.275	0.282	1.40	1.43	25.0	120	4.8	12.6	258.7
	6	0.300	0.300	1.30	1.27	33.2	120	11.4	14.6	345.9

Figures 7 and 8 show the trends of mass of crystals and supersaturation, together with temperature profiles for all runs. The temporal trends of crystal mass in Figure 7 are estimated using the paracetamol concentration in the solution based on the ATR-FTIR measurements. Differences in between values from a mass balance (based on measurements of solution concentration) and weighing product crystals differed by less than 5%, as shown in Table 2.

Table 2: Comparisons of final crystal mass between by scale and by ATR-FTIR

Exp.	measurement of final crystal mass [g]	final crystal mass by ATR-FTIR [g]	Error based on measurement
1	15.6	15.8	1.3%
2	7.2	7.2	0.0%
3	14.2	13.7	-3.5%
4	21.1	21.9	3.8%
5	12.6	13.2	4.8%
6	14.6	14.6	0.0%

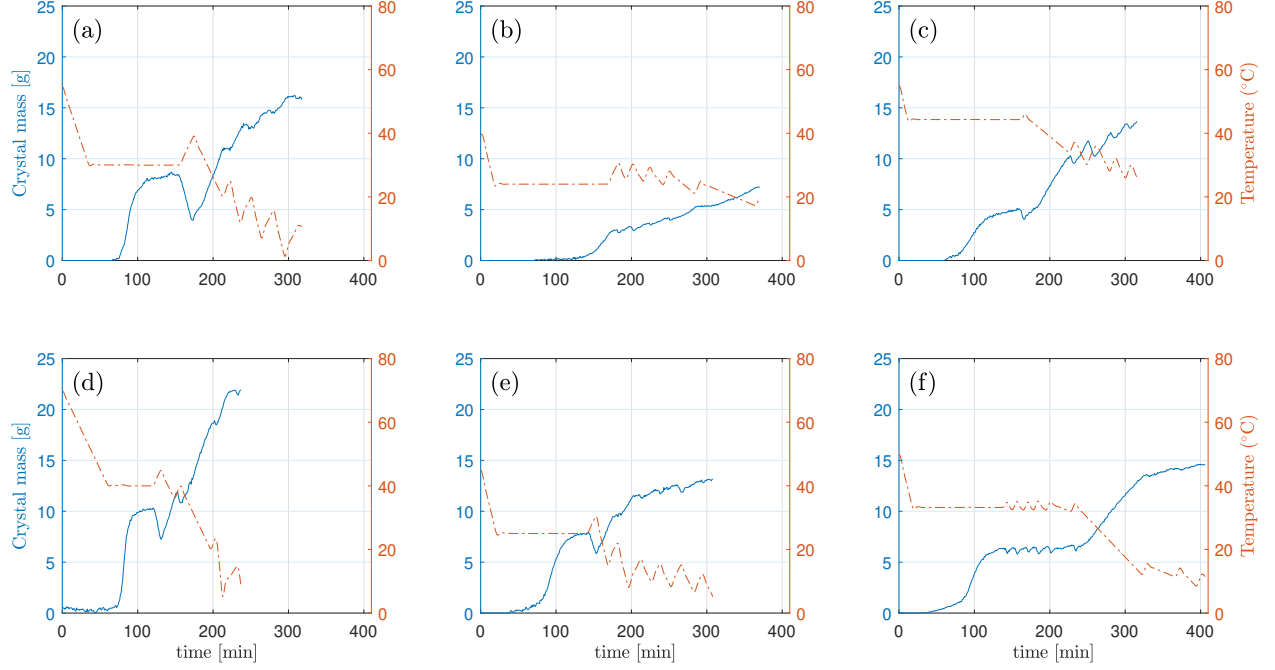


Figure 7: Mass of crystal and temperature profile from crystallization experiments. (a) Exp. 1, (b) Exp. 2, (c) Exp. 3, (d) Exp. 4, (e) Exp. 5, and (f) Exp. 6: blue solid line — supersaturation and red dash-dotted line — temperature profile. Ranges of axes in all figures are fixed based on the largest range among all data sets for easier comparison.

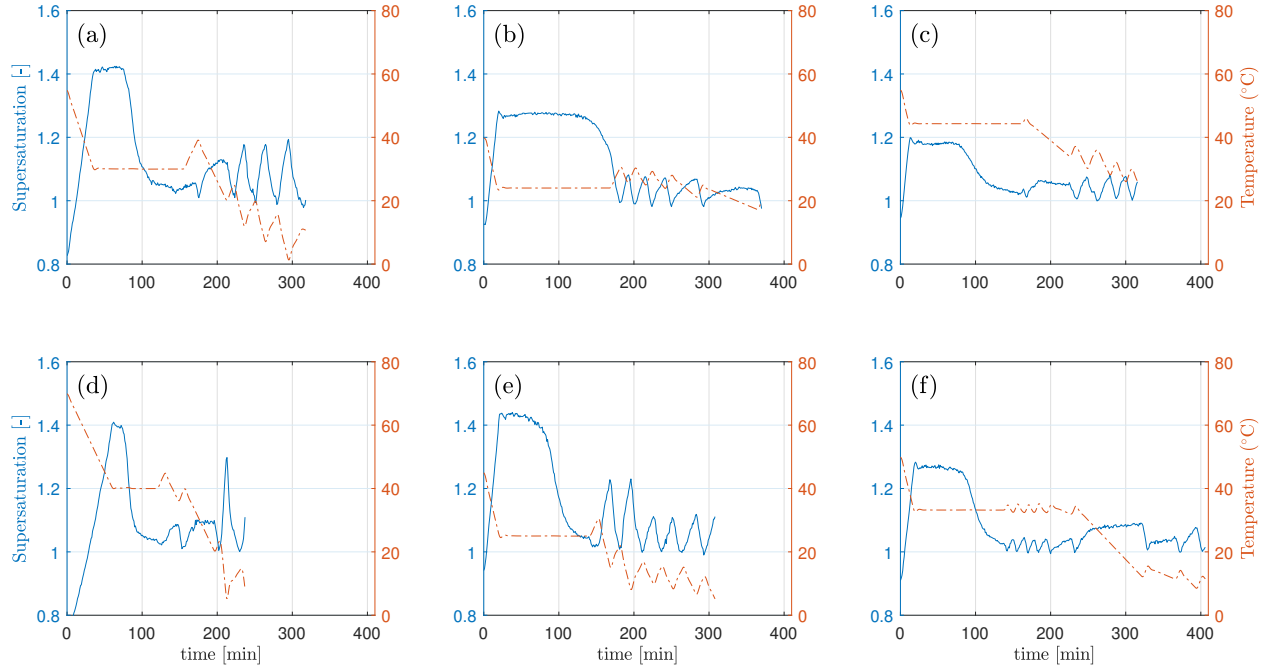


Figure 8: Supersaturation and temperature profile from crystallization experiments. (a) Exp. 1, (b) Exp. 2, (c) Exp. 3, (d) Exp. 4, (e) Exp. 5, and (f) Exp. 6: blue solid line — supersaturation and red dash-dotted line — temperature profile. Ranges of axes in all figures are fixed based on the largest range among all data sets for easier comparison.

Parameter estimation for nucleation, growth, and dissolution

Among six experimental data sets in Table 1, the first three experiments were used as the training set for the parameter estimation and the last three experiments were utilized as the test set. All crystallization experiments were carried out from clear solutions without any seed crystals, so the initial number density distributions are set to zero.

Due to the high non-linearity of the kinetic models, multiple local minima may exist in the optimization problem of parameter estimation. For this problem, **GlobalSearch** and **MultiStart** functions in MATLABTM were applied to identify the global minimum. For rate constants such as k_{b1} , k_{b2} , and k_g , logarithm with base 10 was applied to the parameters to reduce the range of parameter values in the search for optimal solutions.

Table 3: Estimated parameters and confidence intervals for the primary nucleation rate, secondary nucleation rate, and growth rate of crystals

	Parameter	Unit	Value	Confidence interval
Primary nucleation rate	k_{b1}	[#/min/kg solvent]	8.381	8.309–8.454
	σ	[mJ/m ²]	4.174	0.017–8.330
Secondary nucleation rate	k_{b2}	[#/min/kg solvent]	1.346×10^6	$(1.231-1.471) \times 10^6$
	α	[-]	2.650	2.631–2.669
	β	[-]	0.459	0.372–0.547
Growth rate	k_g	$[(\mu\text{m}/\text{min})(\text{g}/\text{g})^{-\gamma_g}]$	1.217×10^9	$(0.974-1.521) \times 10^9$
	$E_{a,g}$	[J/mol]	40300	40300–40300
	γ_g	[-]	1.149	1.145–1.153
Dissolution rate	k_d	$[(\mu\text{m}/\text{min})(\text{g}/\text{g})^{-\gamma_d}]$	4.075×10^4	$(4.075-4.075) \times 10^4$
	$E_{a,d}$	[J/mol]	9800	9800–9800
	γ_d	[-]	0.898	0.874–0.923

Table 3 lists the parameters obtained from the optimization, and Figures 9–11 compare the trends of supersaturation, crystal mass, and the final volume density distributions between experimental data and model fits for the training sets. The calculated profiles of supersaturation and crystal mass based on temperature cycling generally match those in each experimental run. Notably, the model describes the slow consumption of supersaturation in Exp. 2, as shown in Figure 9b.

For validation of obtained kinetic models, three experimental runs, Exp. 4–6 were pre-

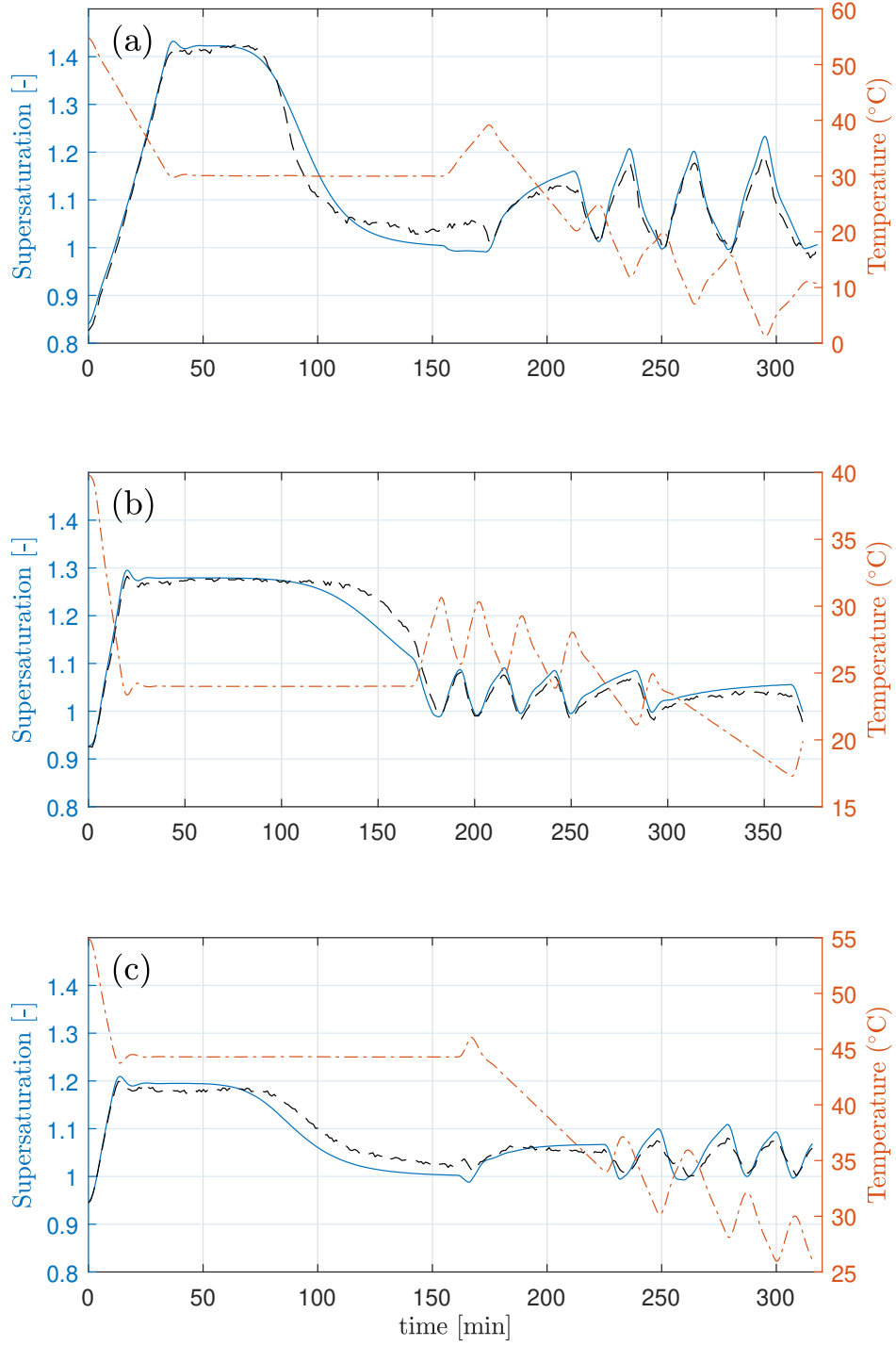


Figure 9: Comparisons of supersaturation between experimental data and fitted results for training sets. (a) Exp. 1, (b) Exp. 2, and (c) Exp. 3: black dashed line — supersaturation from experimental data, blue solid line — supersaturation from model prediction, and red dash-dotted line — temperature profile

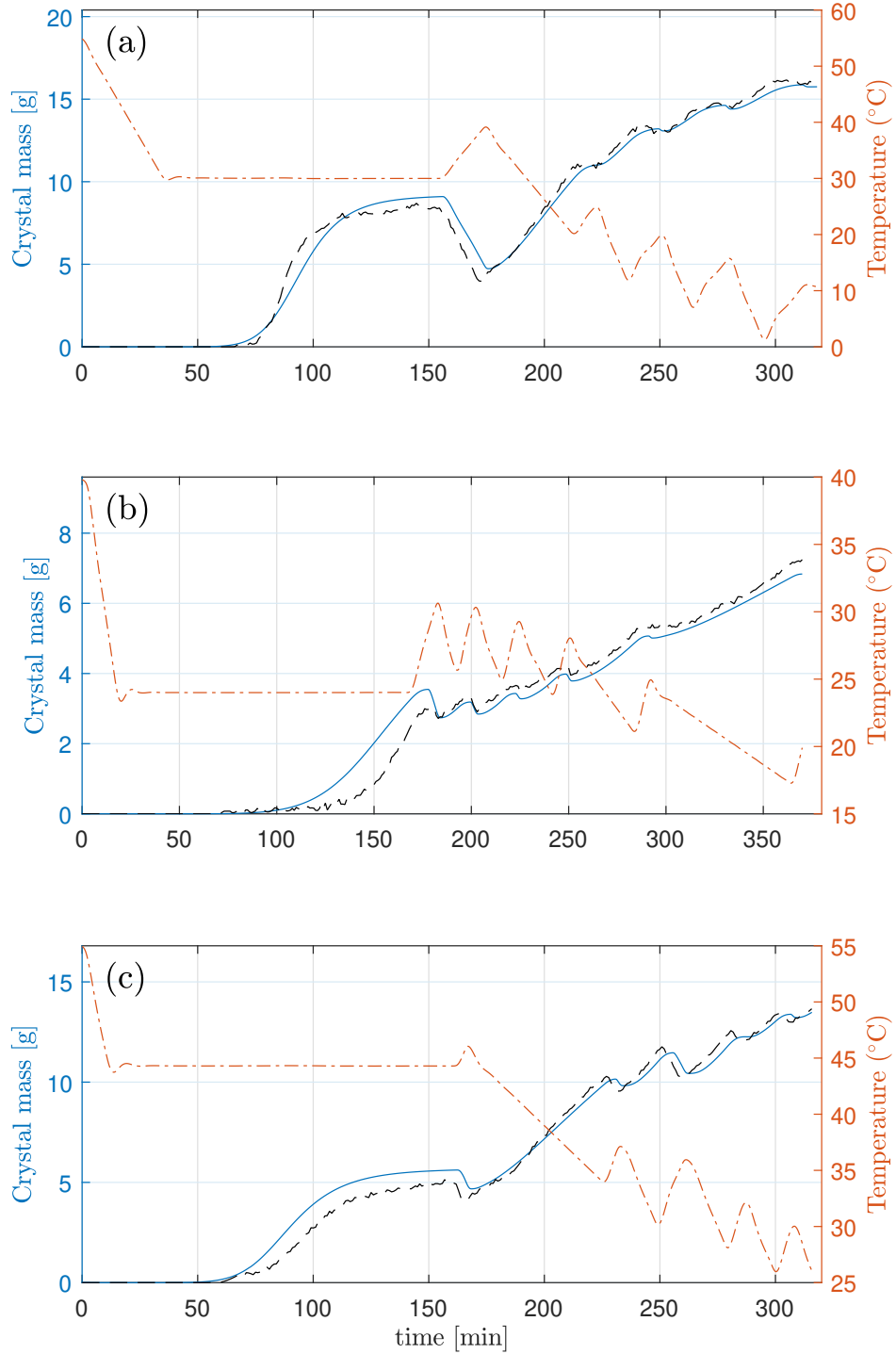


Figure 10: Comparisons of crystal mass between experimental data, as determined from measurements of solution composition and a mass balance, and fitted results for training sets. (a) Exp. 1, (b) Exp. 2, and (c) Exp. 3: black dashed line — crystal mass from experimental data, blue solid line — supersaturation from model prediction, and red dash-dotted line — temperature

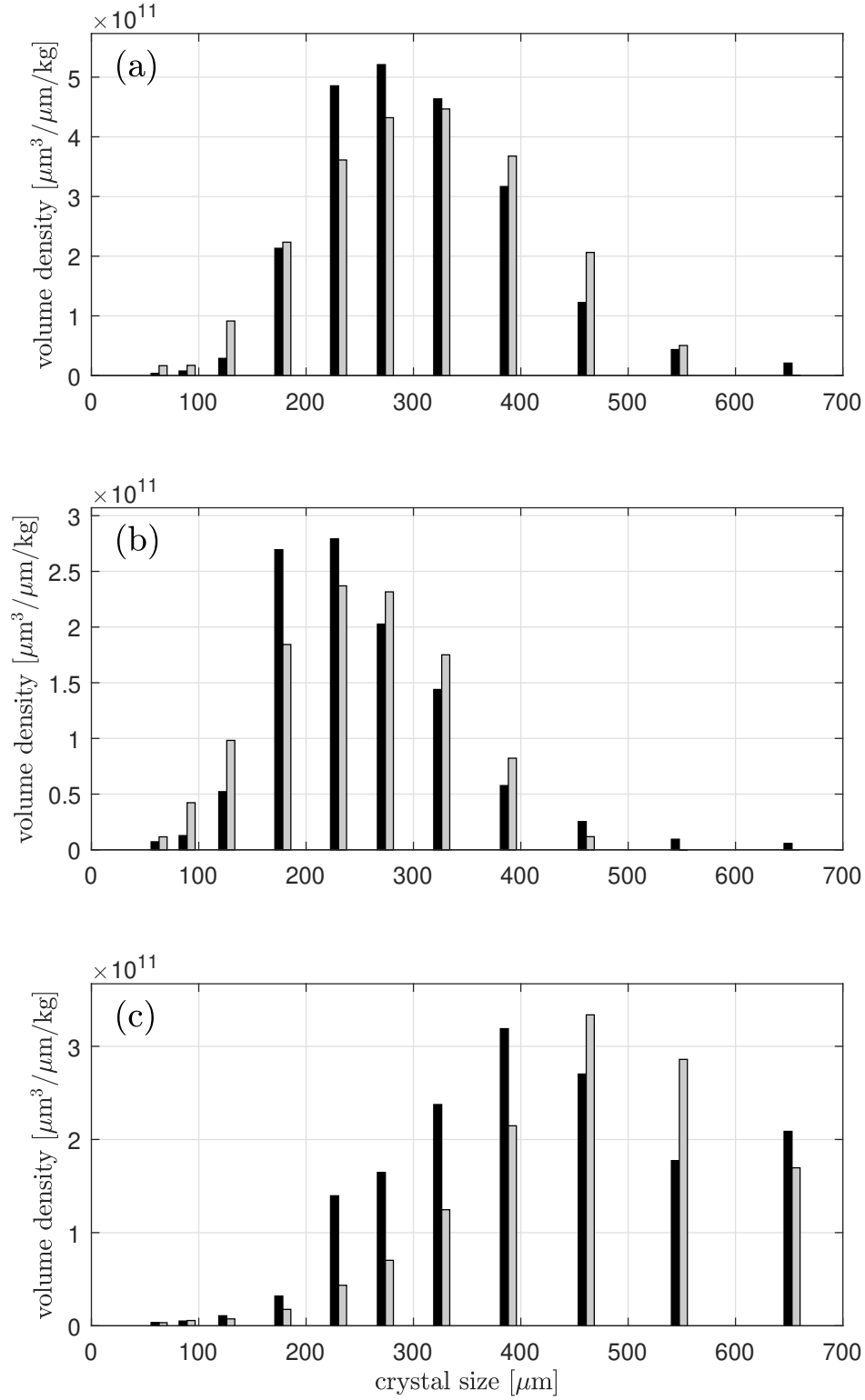


Figure 11: Comparisons of volume density distributions between experimental data and fitted results for training sets. (a) Exp. 1, (b) Exp. 2, and (c) Exp. 3: black bars — experimental data from sieving analysis and gray bars — predicted results from the model

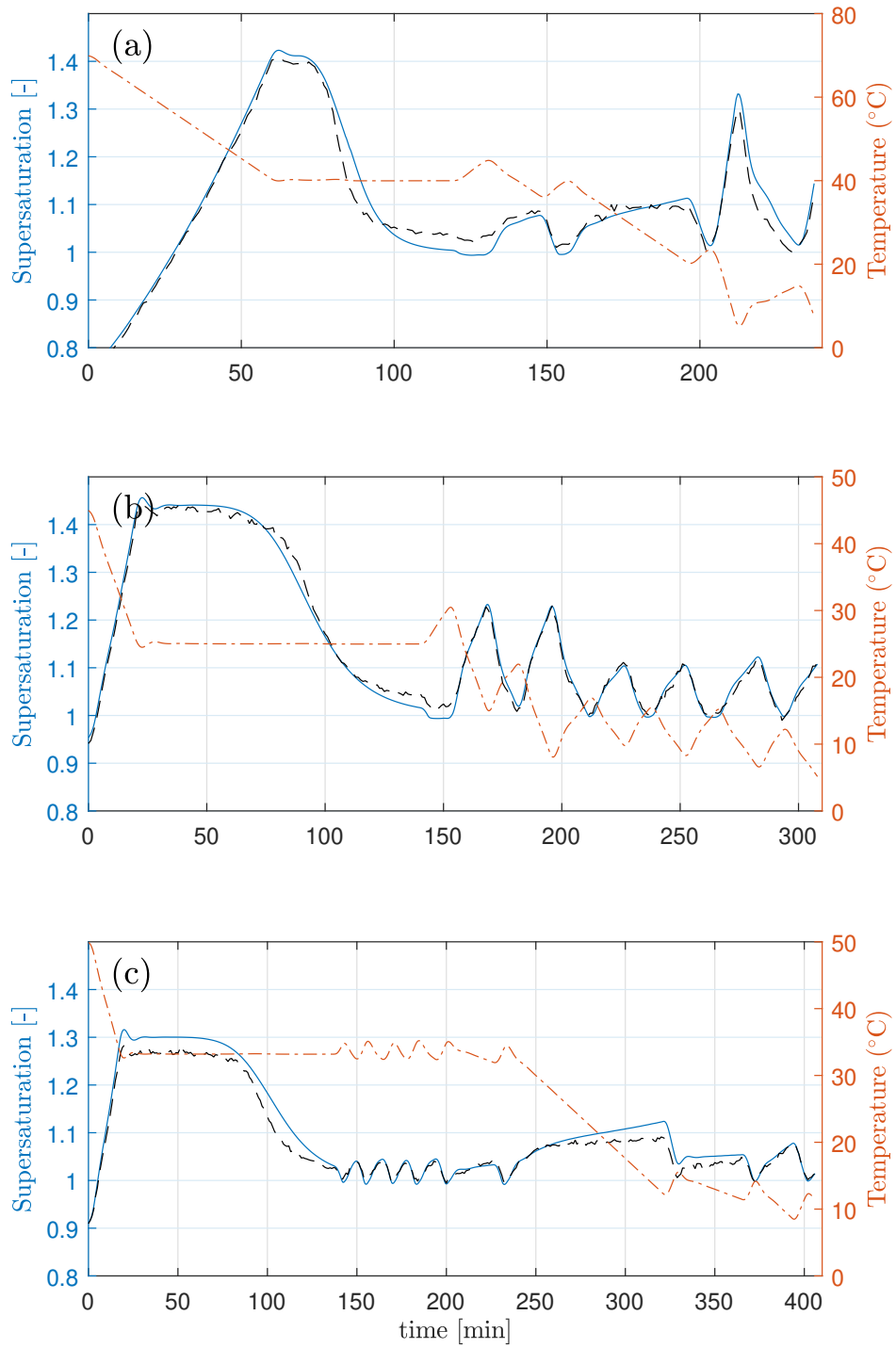


Figure 12: Comparisons of supersaturation between experimental data and predicted results for test sets. (a) Exp. 4, (b) Exp. 5, and (c) Exp. 6: black dashed line — supersaturation from experimental data, blue solid line — supersaturation from model prediction, and red dash-dotted line — temperature profile

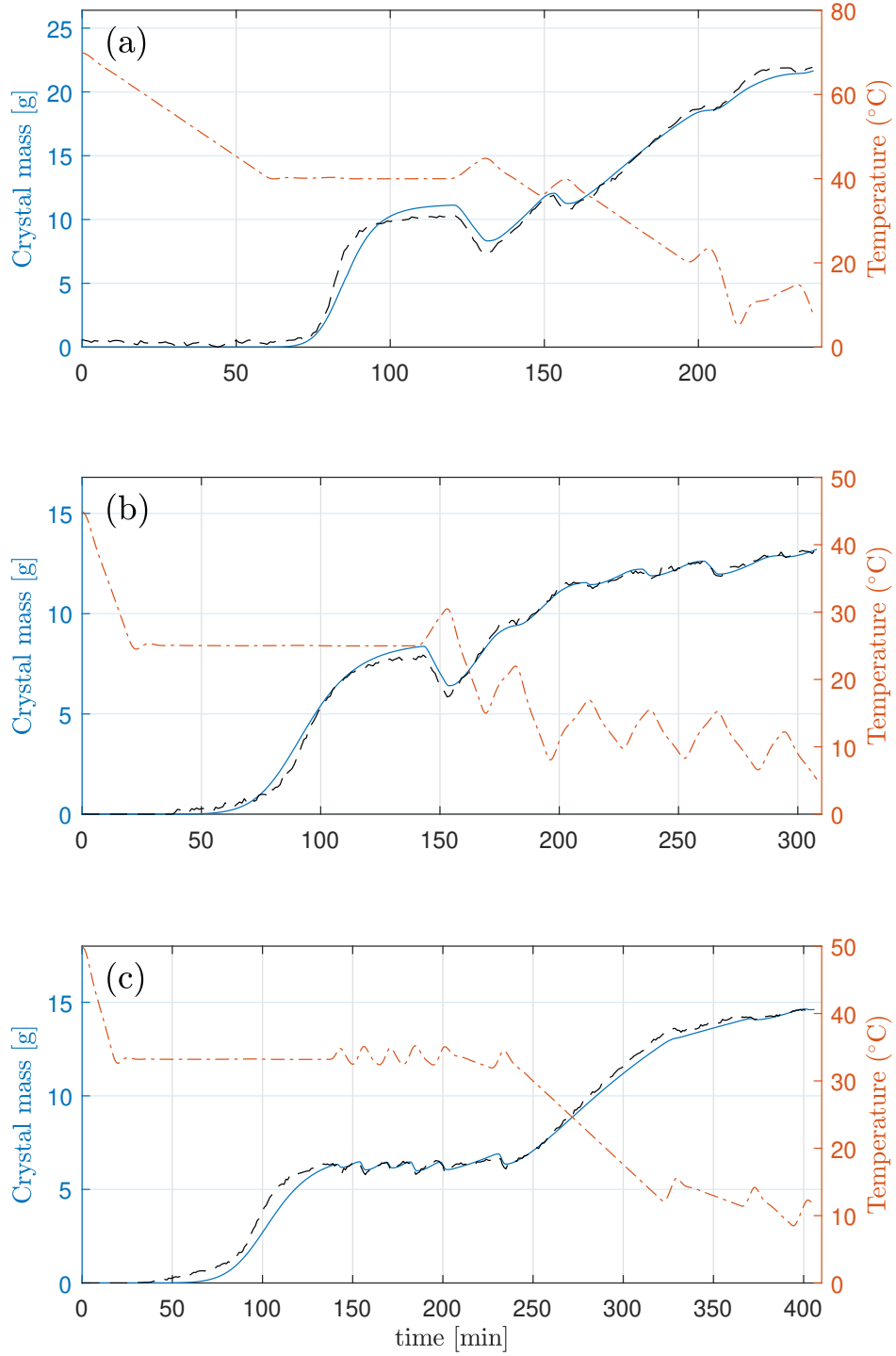


Figure 13: Comparisons of crystal mass between experimental data and predicted results for test sets. (a) Exp. 4, (b) Exp. 5, and (c) Exp. 6: black dashed line — crystal mass from experimental data, blue solid line — supersaturation from model prediction, and red dash-dotted line — temperature

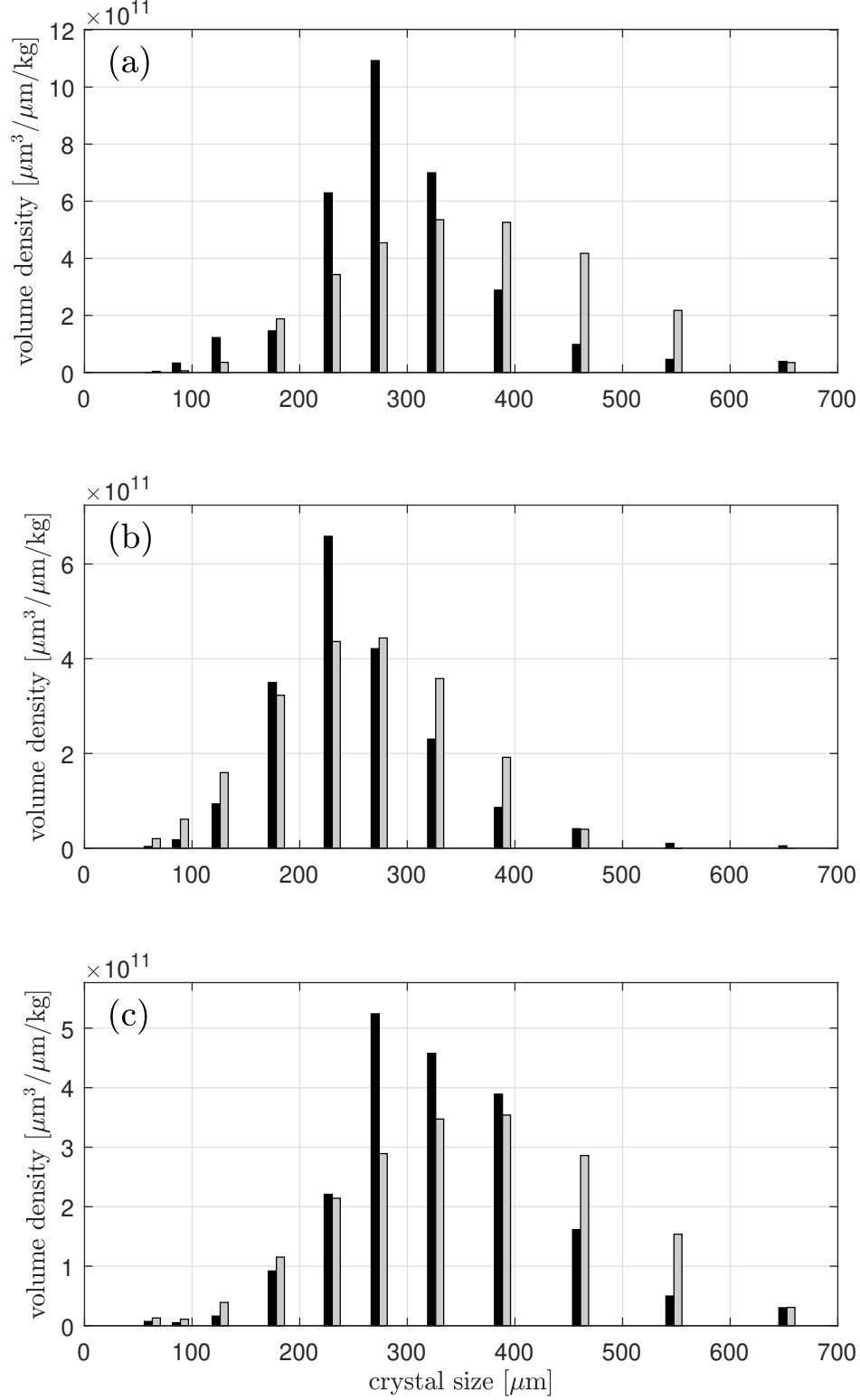


Figure 14: Comparisons of volume density distributions between experimental data, as determined from measurements of solution composition and a mass balance, and predicted results for test sets. (a) Exp. 4, (b) Exp. 5, and (c) Exp. 6: black bars — experimental data from sieving analysis and gray bars — predicted results from the model

dicted, with the conditions of the test sets in Table 1. Predicted supersaturation, crystal mass, and volume density distributions for experiments are compared to the experimental data in Figures 12–14, respectively. The predicted results for Exp. 5 and 6 have reasonable differences from experimental data. However, the prediction of volume density distribution for Exp. 4 tend to be larger than experimental data despite the reasonable match for supersaturation and crystal mass as shown in Figure 14a. In particular, the prediction results for three size ranges, 355–425 μm , 425–500 μm , and 500–600 μm of Exp. 4 have obviously higher values than densities experimentally produced.

Table 4: Comparisons of final mean crystal sizes and span ($d_{90} - d_{10}$) between experiments and simulation

Exp.	volume mean crystal size from experiment [μm]	volume mean crystal size from simulation [μm]	Error based on experimental results
1	317.4	316.8	-0.2%
2	260.0	251.4	-3.3%
3	452.0	498.9	10.4%
4	307.6	369.0	20.0%
5	258.5	261.5	1.1%
6	346.2	372.0	7.4%
Exp.	$d_{90} - d_{10}$ from simulation [μm]	$d_{90} - d_{10}$ from experiment [μm]	Error based on experimental results
1	210.6	252.4	19.9%
2	190.6	213.1	11.8%
3	356.3	312.4	-12.3%
4	179.2	272.1	51.8%
5	177.6	218.2	22.9%
6	213.3	280.7	31.6%

Table 4 lists and compares the volume mean crystal sizes and the span of crystal size distributions from experiments and predicted results. The first term in Equation (10), $\bar{L}_v = \Sigma n_i L_i^4 / \Sigma n_i L_i^3$, estimates the mean crystal size given by the model, and the second term in Equation (10), $\bar{L}_v = \Sigma (M_i L_i) / \Sigma M_i$, calculates mean crystal size measured in the experiments. The span of crystal size distribution was defined as the difference between 90 percentile and 10 percentile to show how broad size distributions are. Errors between mean crystal sizes from experiments and simulations range from -4% to 20%, which may be partly

due to inaccuracies associated with the sieving process. Spans in crystal volume distribution between experiments and predictions show larger errors for test sets, particularly for Exp. 4. The initial experimental concentration, c_{ini} , of Exp. 4 is out of the range of the initial conditions of experiments in the training set, even though the ranges of other experimental conditions in the test set are not too different from the conditions for the training set, as shown in Table 1. Moreover, some crystals may agglomerate during post-crystallization steps such as washing and drying and it may have led to measurement error in the crystal size distributions of the final product. These reasons can cause disagreement on the predicted volume density distribution of Exp. 4. Nonetheless, the errors for the remaining test data is similar to that for the training data, suggesting that the model is predictive.

Discussion

Dissolution modeling

Unlike most models of crystallization processes, our model can describe both the increase and the decrease of the zeroth moment when the temperature increases, which is critical for the temperature-cycling strategy. Figure 15 compares the zeroth and third moments given by the models with and without the scheme to describe crystal disappearance. This comparison was carried out using the temperature profile of Exp. 3. Figure 15a shows that the zeroth and third moments increase and decrease simultaneously. Such behavior occurs when the solution becomes undersaturated as the temperature increases. On the other hand, Figure 15b shows what happens without a disappearance scheme: the zeroth moment does not change while the third moment becomes lower. As the temperature rises and creates undersaturation, existing crystals get smaller so that the total volume of crystals shrinks. However, crystals do not vanish without the disappearance scheme, so the number of crystals does not change.

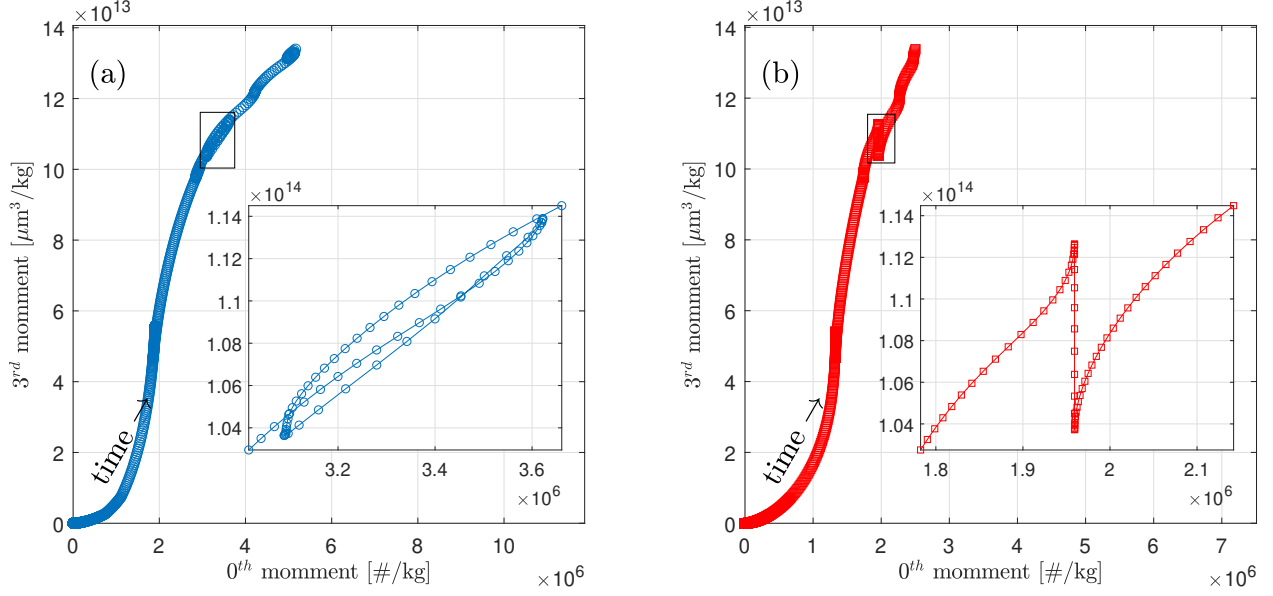


Figure 15: Comparison of trends between the third moment, μ_3 and the zeroth moment, μ_0 for Exp. 3. (a) with the scheme to describe the crystal disappearance and (b) without the scheme. *Inset*: zoomed-in trend for the part in the rectangle.

Prediction of the evolution of volume density distribution

Figure 16 presents predictions for the development of volume density distributions for Exp. 1–6. The absolute volume density increases over time, and the distributions shift toward larger regions. By comparing the volume density change over time with the temperature profiles from Figures 8 and 9, we can also see the volume density decreases when the temperature increases in Figure 16.

Analysis of increasing crystal mass at temperature plateau

Among the crystallization experiments, the supersaturation profile of Exp. 2 showed different behavior from other runs which should be analyzed. In Exp. 2, supersaturation maintained a relatively high value of 1.3 for the relatively long duration in 30–150 minutes, while in all other experiments the supersaturation decreased relatively quickly as shown in Figure 8. To analyze the distinct supersaturation profile in Exp. 2 (Figure 8(b)), we compare the primary nucleation rate, secondary nucleation rate, and growth rate given by the model for cases in

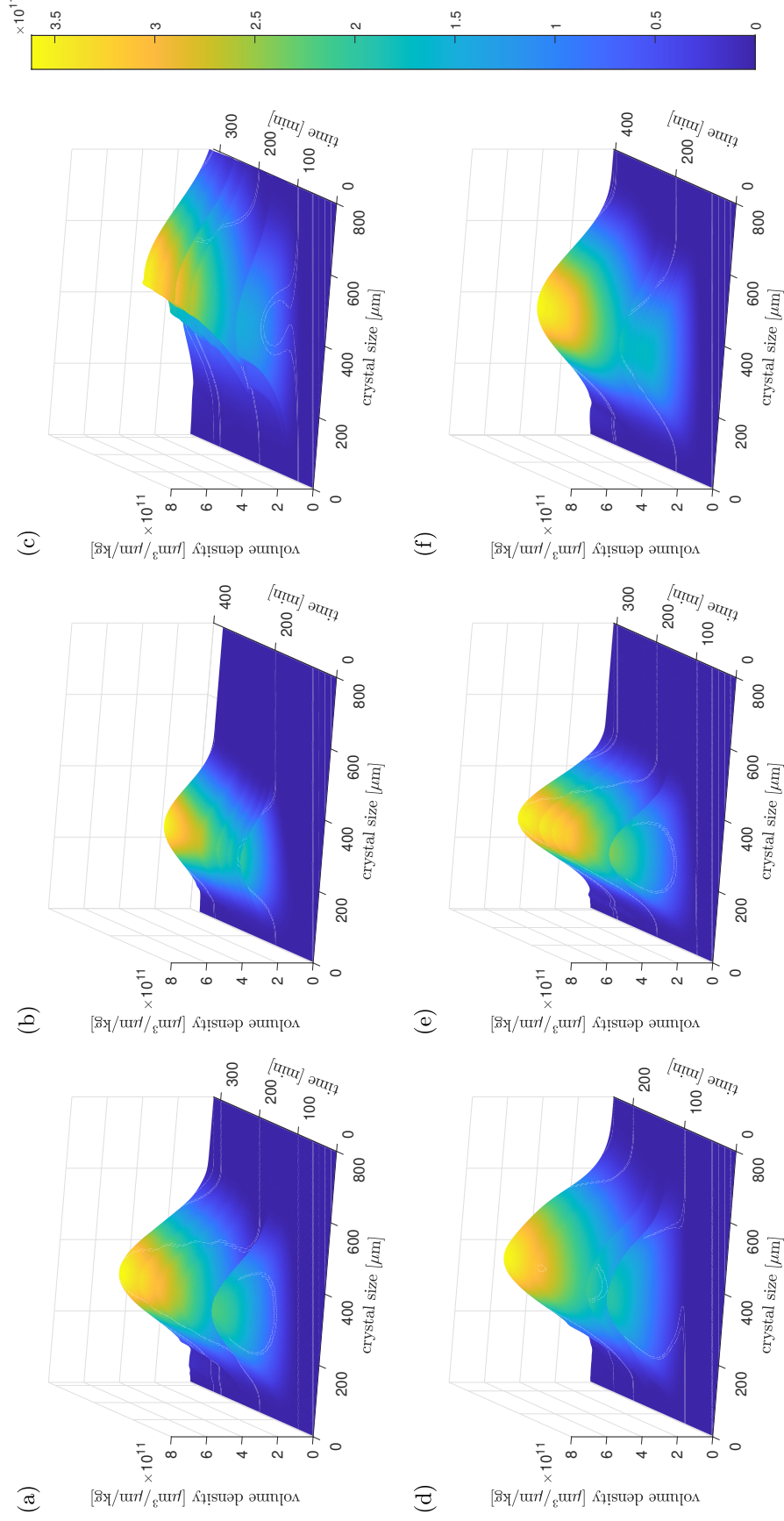


Figure 16: Comparisons of three dimensional volume density distributions. (a)–(f) denote Exp. 1–6, respectively. Colors in the side bar indicate the estimated volume densities

the training set as shown in Figure 17.

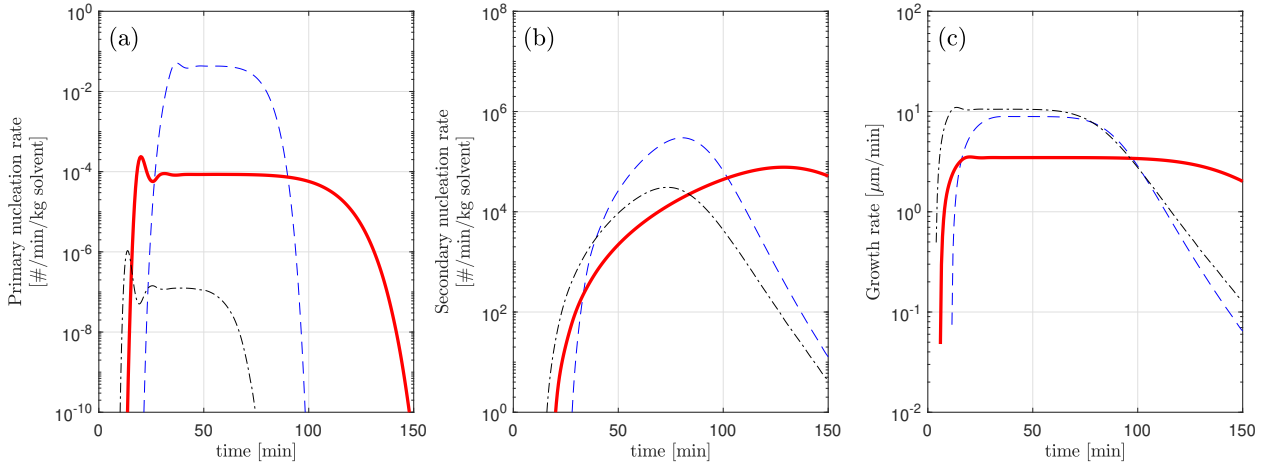


Figure 17: Comparisons of (a) primary nucleation rates, (b) secondary nucleation rates, and (c) growth rates for experimental cases in the training set: blue dashed line — Exp. 1, red solid line — Exp. 2, and black dash-dotted line — Exp. 3.

It can be seen that the secondary nucleation and growth rate in Exp. 2 are the slowest among the three experiments (Figure 17b and c), while the primary nucleation rate is comparable with other experiments (Figure 17a). The slow secondary nucleation rate and growth rate in Exp 2 explain the slow decrease of supersaturation (Figure 8b). In particular, the crystal growth makes the most significant difference because it increases the size of existing crystals, which tends to consume solute molecules more quickly than nucleation which creates only small nuclei.

Conclusions

A mathematical model for unseeded batch crystallization of paracetamol in ethanol solutions was developed that includes primary and secondary nucleation, growth, dissolution, and disappearance of crystals. The approach employed a bin of negative size to describe the disappearance of crystals during the dissolution process. As dissolution moved crystals into this negative bin they were deemed to have disappeared and no longer were part of the population balance model. Parameter estimation for the rates of primary nucleation,

secondary nucleation, growth, and dissolution was carried out at the same time because the key phenomena cannot be observed separately. The developed model was validated using experimental data from three unseeded batch crystallizations that followed the temperature-cycling strategy.

This model can account for the dissolution and disappearance of crystals when the temperature rises, and we verified that the developed model works reasonably by comparing the behavior of the moments when the temperature-cycling strategy was employed. Therefore, this model can be used to explain and analyze the evolution of a crystal population density distribution when heating and cooling are part of the crystallization protocol. In addition, this model was conducive to analyze nucleation and growth rates separately to look for the reason for the experimental observation where supersaturation profiles differ significantly under some experimental conditions. A model using the principles developed in the present work will be a powerful tool whose utilization will facilitate optimization of batch cooling crystallization processes that employ the temperature-cycling strategy.

Acknowledgement

This work was supported in the form of a student fellowship for Youngjo Kim by the Hanwha Solutions Corporation.

Supporting Information Available

- Details on the determination of initial guess of dissolution parameters and comparison of the dissolution rates using the model in Worlitschek and Mazzotti¹⁴

References

- (1) Tavaré, N. S. *Industrial Crystallization: Process Simulation Analysis and Design*; The Plenum Chemical Engineering Series; Springer US, 1995.
- (2) Myerson, A. S.; Erdemir, D.; Lee, A. Y. *Handbook of Industrial Crystallization*, 3rd ed.; Cambridge University Press, 2019.
- (3) Nagy, Z. K.; Aamir, E.; Rielly, C. D. Internal fines removal using population balance model based control of crystal size distribution under dissolution, growth and nucleation mechanisms. *Cryst. Growth Des.* **2011**, *11*, 2205–2219.
- (4) Saleemi, A.; Rielly, C.; Nagy, Z. K. Automated direct nucleation control for in situ dynamic fines removal in batch cooling crystallization. *CrystEngComm* **2012**, *14*, 2196–2203.
- (5) Griffin, D. J.; Grover, M. A.; Kawajiri, Y.; Rousseau, R. W. Data-driven modeling and dynamic programming applied to batch cooling crystallization. *Ind. Eng. Chem. Res.* **2016**, *55*, 1361–1372.
- (6) Griffin, D. J.; Kawajiri, Y.; Rousseau, R. W.; Grover, M. A. Using MC plots for control of paracetamol crystallization. *Chem. Eng. Sci.* **2017**, *164*, 344–360.
- (7) Lovette, M. A.; Muratore, M.; Doherty, M. F. Crystal shape modification through cycles of dissolution and growth: Attainable regions and experimental validation. *AIChE J.* **2011**, *58*, 1465–1474.
- (8) Jiang, M.; Zhu, X.; Molaro, M. C.; Rasche, M. L.; Zhang, H.; Chadwick, K.; Raimondo, D. M.; Kim, K. K. K.; Zhou, L.; Zhu, Z.; Wong, M. H.; O’Grady, D.; Hebrault, D.; Tedesco, J.; Braatz, R. D. Modification of crystal shape through deep temperature cycling. *Ind. Eng. Chem. Res.* **2014**, *53*, 5325–5336.

- (9) Doki, N.; Seki, H.; Takano, K.; Asatani, H.; Yokota, M.; Kubota, N. Process control of seeded batch cooling crystallization of the metastable α -form glycine using an in-situ ATR-FTIR spectrometer and an in-situ FBRM particle counter. *Cryst. Growth Des.* **2004**, *4*, 949–953.
- (10) Abu Bakar, M. R.; Nagy, Z. K.; Rielly, C. D. Seeded batch cooling crystallization with temperature cycling for the control of size uniformity and polymorphic purity of sulfathiazole crystals. *Org. Process Res. Dev.* **2009**, *13*, 1343–1356.
- (11) Suwannasang, K.; Flood, A. E.; Rougeot, C.; Coquerel, G. Using programmed heating–cooling cycles with racemization in solution for complete symmetry breaking of a conglomerate forming system. *Cryst. Growth Des.* **2013**, *13*, 3498–3504.
- (12) Breveglieri, F.; Maggioni, G. M.; Mazzotti, M. Deracemization of NMPA via temperature cycles. *Cryst. Growth Des.* **2018**, *18*, 1873–1881.
- (13) Wu, Z.; Yang, S.; Wu, W. Application of temperature cycling for crystal quality control during crystallization. *CrystEngComm* **2016**, *18*, 2222–2238.
- (14) Worlitschek, J.; Mazzotti, M. Model-based optimization of particle size distribution in batch-cooling crystallization of paracetamol. *Cryst. Growth Des.* **2004**, *4*, 891 – 903.
- (15) Gherras, N.; Fevotte, G. On the use of process analytical technologies and population balance equations for the estimation of crystallization kinetics. A case study. *AIChE J.* **2012**, *58*, 2650–2664.
- (16) Ó’Ciardhá, C. T.; Hutton, K. W.; Mitchell, N. A.; Frawley, P. J. Simultaneous parameter estimation and optimization of a seeded antisolvent crystallization. *Cryst. Growth Des.* **2012**, *12*, 5247–5261.
- (17) Li, H.; Kawajiri, Y.; Grover, M. A.; Rousseau, R. W. Modeling of nucleation and

- growth kinetics for unseeded batch cooling crystallization. *Ind. Eng. Chem. Res.* **2017**, *56*, 4060–4073.
- (18) Trampuž, M.; Teslić, D.; Likozar, B. Crystallization of fesoterodine fumarate active pharmaceutical ingredient: Modelling of thermodynamic equilibrium, nucleation, growth, agglomeration and dissolution kinetics and temperature cycling. *Chem. Eng. Sci.* **2019**, *201*, 97–111.
- (19) Shoji, M.; Eto, T.; Takiyama, H. A kinetic study of the influence of modulated undersaturation operation on crystal size distribution in cooling-type batch crystallization. *J. Chem. Eng. Jpn.* **2011**, *44*, 191–196.
- (20) Seki, H.; Furuya, N.; Hoshino, S. Evaluation of controlled cooling for seeded batch crystallization incorporating dissolution. *Chem. Eng. Sci.* **2012**, *77*, 10–17.
- (21) Mao, S.; Zhang, Y.; Rohani, S.; Ray, A. K. Kinetics of (R,S)- and (R)-mandelic acid in an unseeded cooling batch crystallizer. *J. Cryst. Growth* **2010**, *312*, 3340–3348.
- (22) Frawley, P. J.; Mitchell, N. A.; Ó’Ciardhá, C. T.; Hutton, K. W. The effects of supersaturation, temperature, agitation and seed surface area on the secondary nucleation of paracetamol in ethanol solutions. *Chem. Eng. Sci.* **2012**, *75*, 183–197.
- (23) Yang, Y.; Nagy, Z. K. Advanced control approaches for combined cooling/antisolvent crystallization in continuous mixed suspension mixed product removal cascade crystallizers. *Chem. Eng. Sci.* **2015**, *127*, 362–373.
- (24) Kumar, S.; Ramkrishna, D. On the solution of population balance equations by discretization — III. Nucleation, growth and aggregation of particles. *Chem. Eng. Sci.* **1997**, *52*, 4659–4679.
- (25) Porru, M.; Özkan, L. Monitoring of batch industrial crystallization with growth, nucle-

- ation, and agglomeration. Part 1: Modeling with method of characteristics. *Ind. Eng. Chem. Res.* **2017**, *56*, 5980–5992.
- (26) Wulkow, M.; Gerstlauer, A.; Nieken, U. Modeling and simulation of crystallization processes using parsival. *Chem. Eng. Sci.* **2001**, *56*, 2575–2588.
- (27) Gunawan, R.; Fusman, I.; Braatz, R. D. High resolution algorithms for multidimensional population balance equations. *AIChE J.* **2004**, *50*, 2738–2749.
- (28) Gunawan, R.; Fusman, I.; Braatz, R. D. Parallel high-resolution finite volume simulation of particulate processes. *AIChE J.* **2008**, *54*, 1449–1458.
- (29) Sulttan, S.; Rohani, S. Coupling of CFD and population balance modelling for a continuously seeded helical tubular crystallizer. *J. Cryst. Growth* **2019**, *505*, 19–25.
- (30) Motz, S.; Mitrović, A.; Gilles, E. Comparison of numerical methods for the simulation of dispersed phase systems. *Chem. Eng. Sci.* **2002**, *57*, 4329–4344.
- (31) Qamar, S.; Elsner, M. P.; Angelov, I. A.; Warnecke, G.; Seidel-Morgenstern, A. A comparative study of high resolution schemes for solving population balances in crystallization. *Comput. Chem. Eng.* **2006**, *30*, 1119–1131.
- (32) Randolph, A. D.; Larson, M. A. *Theory of Particulate Processes: Analysis and Techniques of Continuous Crystallization*; Elsevier Science, 2012.
- (33) Ottens, E. P.; Janse, A. H.; De Jong, E. J. Secondary nucleation in a stirred vessel cooling crystallizer. *J. Cryst. Growth* **1972**, *13-14*, 500–505.
- (34) Evans, T. W.; Sarofim, A. F. Models of secondary nucleation attributable. *AIChE J.* **1974**, *20*, 959–966.
- (35) Liiri, M.; Koironen, T.; Aittamaa, J. Secondary nucleation due to crystal-impeller and crystal-vessel collisions by population balances in CFD-modelling. *J. Cryst. Growth* **2002**, *237-239*, 2188–2193.

- (36) Agrawal, S. G.; Paterson, A. H. Secondary nucleation: Mechanisms and models. *Chem. Eng. Commun.* **2015**, *202*, 698–706.
- (37) Seki, H.; Su, Y. Robust optimal temperature swing operations for size control of seeded batch cooling crystallization. *Chem. Eng. Sci.* **2015**, *133*, 16–23.
- (38) Chang, S.-C. The method of space-time conservation element and solution element — A new approach for solving the Navier-Stokes and Euler equations. *J. Comput. Phys.* **1995**, *119*, 295–324.
- (39) Jiang, C.; Feng, X.; Zhang, J.; Zhong, D. AMR simulations of magnetohydrodynamic problems by the CESE method in curvilinear coordinates. *Sol. Phys.* **2010**, *267*, 463–491.
- (40) Ayasoufi, A.; Keith, T. G.; Rahmani, R. K. Application of the conservation element and solution element method in numerical modeling of three-dimensional heat conduction with melting and/or freezing. *J. Heat Transfer* **2004**, *126*, 937–945.
- (41) Chou, Y.; Yang, R. J. Two-dimensional Dual-Phase-Lag thermal behavior in single-/multi-layer structures using CESE method. *Int. J. Heat Mass Transfer* **2009**, *52*, 239–249.
- (42) Lim, Y. I.; Jorgensen, S. B. A fast and accurate numerical method for solving simulated moving bed (SMB) chromatographic separation problems. *Chem. Eng. Sci.* **2004**, *59*, 1931–1947.
- (43) Lim, Y. I.; Lee, J.; Bhatia, S. K.; Lim, Y. S.; Han, C. Improvement of para-Xylene SMB process performance on an industrial scale. *Ind. Eng. Chem. Res.* **2010**, *49*, 3316–3327.
- (44) Ward, J. D.; Yu, C. C. Population balance modeling in Simulink: PCSS. *Chem. Eng. Sci.* **2008**, *32*, 2233–2242.

- (45) Noor, S.; Qamar, S. The space time CE/SE method for solving one-dimensional batch crystallization model with fines dissolution. *Chin. J. Chem. Eng.* **2015**, *23*, 337–341.
- (46) Mullin, J. W. *Crystallization*, 4th ed.; Butterworth-Heinemann, 2001; pp 1–594.
- (47) Nocedal, J.; Wright, S. J. *Numerical Optimization*; Springer, 2006.
- (48) Bard, Y. *Nonlinear Parameter Estimation*; Academic Press, 1974.
- (49) Rawlings, J. B.; Miller, S. M.; Witkowski, W. R. Model identification and control of solution crystallization processes: A review. *Ind. Eng. Chem. Res.* **1993**, *32*, 1275–1296.
- (50) Cornel, J.; Lindenberg, C.; Mazzotti, M. Quantitative application of in-situ ATR-FTIR and Raman spectroscopy in crystallization processes. *Ind. Eng. Chem. Res.* **2008**, *47*, 4870–4882.
- (51) Nikolic, G. *Fourier Transforms: New Analytical Approaches and FTIR Strategies*; Intech, 2011.
- (52) Griffin, D. J.; Grover, M. A.; Kawajiri, Y.; Rousseau, R. W. Robust multicomponent IR-to-concentration model regression. *Chem. Eng. Sci.* **2014**, *116*, 77–90.
- (53) Chianese, A. Characterization of crystal size distribution. *Ind. Cryst. Process Monit. Control* **2012**, 1–6.
- (54) Li, H.; Kawajiri, Y.; Grover, M. A.; Rousseau, R. W. Application of an empirical FBRM model to estimate crystal size distributions in batch crystallization. *Cryst. Growth Des.* **2014**, *14*, 607–616.

Graphical TOC Entry

